

# Towards Sustainable Haptics: A Wearable Vibrotactile Solar-Powered System with Biodegradable Components

*Robin Arbaud<sup>1</sup>, Maedeh Najafi<sup>2</sup>, Juan M. Gandarias<sup>1</sup>, Marta Lorenzini<sup>1</sup>, Uttam C. Paul<sup>2</sup>, Arkadiusz Zych<sup>2</sup>, Athanassia Athanassiou<sup>2</sup>, Pietro Cataldi<sup>\*2</sup>, Arash Ajoudani<sup>\*1</sup>*

<sup>1</sup> R. Arbaud, J. M. Gandarias, M. Lorenzini, A. Ajoudani

Human-Robot Interfaces and Interaction, Istituto Italiano di Tecnologia, Genoa, Italy.

\*Email Address: arash.ajoudani@iit.it

<sup>2</sup> M. Najafi, U. C. Paul, A. Zych, A. Athanassiou, P. Cataldi

Smart Materials Laboratory, Istituto Italiano di Tecnologia, Genoa, Italy.

\*Email Address: pietro.cataldi@iit.it

**Keywords:** *Green Mechatronics, Sustainable Haptics, Conductive Inks, Vibrotactile Feedback, Green Electronics*

Electronics and mechatronics waste is an exponentially increasing environmental issue, especially for wearable devices, due to their widespread diffusion into society and short life cycle. To promote their enormous benefits (e.g., in assisting visually-impaired individuals) in a sustainable way, biobased and/or biodegradable organic materials should be used instead of traditional components. This manuscript presents our multidisciplinary approach, which bridges materials science and mechatronics, to propose the first ECO-friendly wearable vibroTACtile device (Eco-Tac). The design of Eco-Tac includes integration on a cotton T-Shirt through a novel biodegradable conductive ink forming electrical tracks, a flexible commercially available solar panel, and the vibrotactile haptic device itself. The ink comprises a nonconventional green solvent, anisole, a soft polybutylene adipate terephthalate biodegradable binder, and conductive nanocarbon materials. The device case is a biodegradable biocomposite. As such, the feasibility of using a sustainable energy source to supply power to the device and the possibility of using biodegradable materials in its manufacturing are demonstrated. An experiment with twenty blindfolded subjects is conducted, reporting the device's potential for assistance in manipulation tasks. Overall, the results of this work represent the first significant step towards the creation of wearable and sustainable haptic devices with green electronics and mechatronics approaches.

## 1 Introduction

The recent advancements in robotics [1, 2] and artificial intelligence [3, 4, 5] have brought many benefits to society, ranging from improved manufacturing [1] to enhanced medical procedures [3]. However, as the demand for new technologies rises, so does the amount of electronic waste (*e-waste*) and other robotic and mechatronics waste generated [6, 7]. Most electronic and mechatronic components are made of plastics, composites, metals, batteries, sensors, actuators, etc. constructed from inorganic, cumbersome, rigid, and sometimes rare materials that last hundreds or even a thousand years in the environment if not disposed of correctly [8, 7]. In addition, they usually include harmful compounds such as heavy metals, brominated flame retardants, and polyhalogenated molecules that may be released into the environment [9]. As such, disposal of the generated waste is exceptionally complicated. The irruption of environmentally friendly electronics, mechatronics, and robotics systems will be pivotal for the sustainable long-term development of numerous sectors [7, 10].

Wearable devices, especially, are becoming increasingly popular due to their potential of use in several application domains, such as healthcare, sports, energy, and robotics [11, 12, 13, 14, 15, 16]. Their nature makes them a perfect subject for applying eco-friendly practices that may become a standard for the entire electronics, mechatronics, and robotics sector since those applications that exploit this technology share the following common features:

1. The number of devices per application is usually high.
2. Their life cycle is usually short.
3. They are assembled with small and generally cheap plastic and electronic components that can easily end up in the environment by mistake and damage it.

Consequently, the amount of waste per device may be higher and even more harmful than other technologies.

A large number of haptic feedback devices are wearable systems built with classic long-lasting and unsustainable electronic and robotic components whose primary advantage is providing touch-like sensations for those who have lost it [17] or sensory substitutions for situational awareness or guidance [18]. These advantages are particularly useful in prosthetics, as amputees often struggle to regain a sense of touch [19, 20]. With wearable haptics, the wearers can exploit artificial haptic feedback by feeling vibrations and tactile sensations that mimic natural touch to improve performance in several tasks. As such, individuals are helped to adapt to their prosthetics, improve their movements, and better manage their activities of daily living [21]. Another factor that may help impaired people to adapt to their prosthetics is the design of wearable systems on platforms with which they are already familiar such as textile T-shirts, gloves, or other ordinary clothes. The long-term vision is the integration of wearable haptic feedback devices through flexible, soft, and imperceptible materials that maximize the wearer's comfort. Other advantages of haptic feedback devices include enhancing human-robot interactions [22], improving virtual and augmented reality experiences [23], enhancing sports performances [24], and assisting visually impaired people in navigating the environment [25]. The latter, in particular, has been shown to impact their independence, mobility, and confidence significantly. While most of the existing works in this topic focus on using haptic devices for navigation and locomotion guidance, their usage for manipulation tasks has yet to be investigated.

In light of the vast exploitation potential of wearable haptic devices on a large scale, eco-friendly design principles, such as using biobased and/or biodegradable materials should be considered to promote sustainability. These approaches and materials, which have many additional desirable properties such as being organic, natural, flexible, and lightweight, contributing in improving the comfort of the wearer, are advisable to reduce the environmental impact during production, e.g., decreasing the generated CO<sub>2</sub>, the toxic chemicals employed during production, and the energy consumption. Moreover, they could simplify e-waste management, e.g., through more straightforward disposal of the components at the end of use. They can help reduce the percentage of non-degradable materials accidentally discarded in the environment if some devices are not disposed of correctly.

Wearable electrically conductive materials/tracks are also crucial for integrating components in wearable haptic devices and signal and power transmission. Electrically conductive wearable tracks are frequently made by weaving and knitting metal wires into textiles [26, 27, 28]. However, metals lack the wearability, flexibility, and washability required in such applications [26], which can decrease the wearer's comfort. Coating and functionalizing standard fabrics such as T-shirts with conductive inks/pastes are another popular approach that is interesting for wearable haptics devices. Indeed this strategy enables the direct integration of the different electronic components or sensors onto the fabric [26, 29, 30, 31, 32, 33, 34, 35, 36], improving the comfort and familiarity of the patient with the haptic device. Widespread methods that allow covering large textiles areas quickly, such as dip-, spray-, blade-coating, and screen printing, are desirable and efficient using conductive inks and pastes [29, 28, 35]. These inks are usually manufactured using binders and surfactants that are frequently not eco-friendly, sustainable, or quickly biodegradable. Typically, organic nanocarbons, conductive polymers, or micro and nanoscale metals supply the conductivity [37, 38, 39, 27, 33, 35]. Nanocarbons shine for their range of structures (i.e., 1D, 2D, or 3D), low cost, lightweight, and dispersibility in environmentally friendly solvents when compared to nanometals and conductive polymers [40, 41, 42, 43, 44, 45]. Carbon nanofibers ensure tens of tons scale availability and affordable pricing compared to fullerene, single-wall carbon nanotubes (CnTs), or single-layer graphene [40, 32, 42, 43, 44, 45]. Another benefit, especially of 1D nanocarbons, is their high aspect ratio, which provides an excellent electrical percolation network at low loadings [40, 42, 43, 44, 35, 45].

Electronic textiles that utilize natural textiles as substrates and biodegradable biopolymers as matrices/binders of the conductive fillers are increasingly studied in the quest for environmental friendliness [46, 47, 48, 49]. These materials are appropriate for green electronics and robotics due to their sustainability, biodegradability, and natural abundance [46, 47, 50, 48]. Nevertheless, using biopolymers is more com-

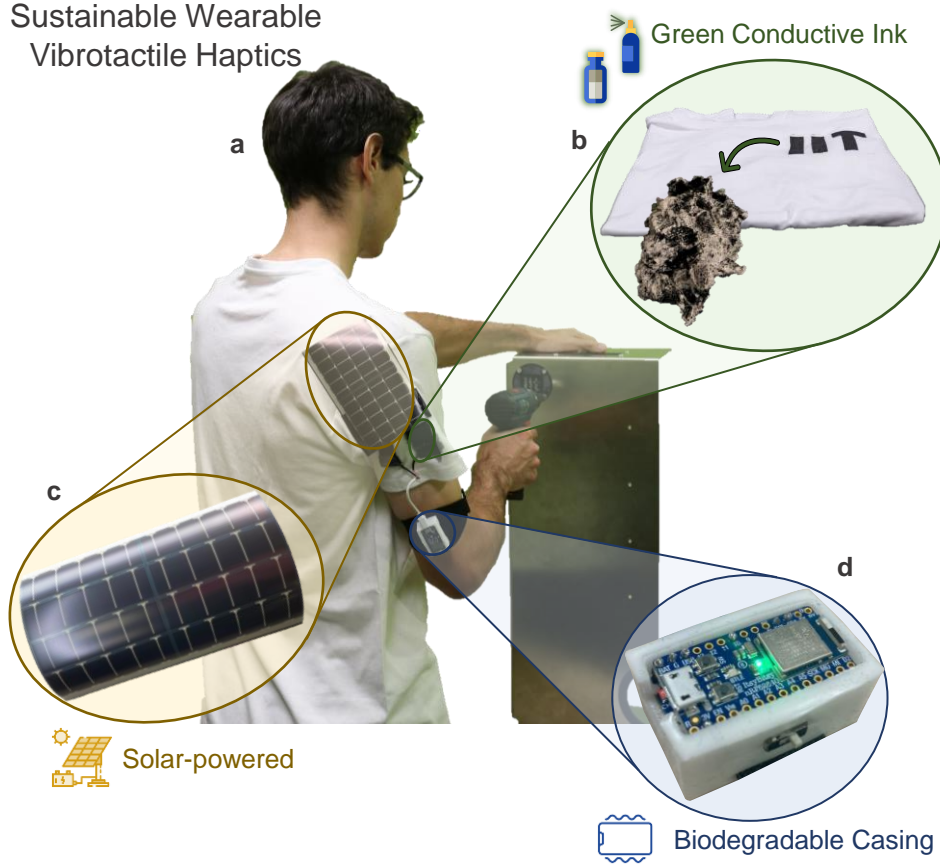


**Figure 1: Illustration of the first ECO-friendly wearable vibrotactile device (Eco-Tac) system at work.** (a) A worker during a drilling operation wearing the Eco-Tac. (b) Green conductive ink deposited on a T-shirt and the obtained material after biological oxygen demand degradation test in seawater. (c) A flexible solar power source integrated onto the T-shirt employing the conductive tracks of (b). (d) The Eco-Tac device, comprising commercially available electronics in a flexible and stretchable biodegradable case and powered by the flexible solar power source through the degradable conductive tracks.

plex than using standard durable materials since they are not designed to survive significant mechanical deformation and washing cycles [51, 48, 52]. Many works in this field either do not mention washability or guarantee it by covering the material in a non-degradable plastic [38]. Moreover, the biodegradability of the final composite material is rarely tested.

Polybutylene adipate terephthalate (PBAT) is a thermoplastic biopolymer already large-scale produced by companies such as BASF and Novamont, and, as such, its volume of production is already compatible with market requests and the polymer/electronics/robotics industries [53, 54]. It is biodegradable due to the aliphatic unit in its molecular chain, but it also possesses high mechanical properties due to the aromatic unit [55]. Indeed, PBAT is more flexible than poly (lactic acid) (PLA) and poly (butylene-succinate) and could be used as a substitute for low-density polyethylene [53, 54]. So far, PBAT is mainly used to improve the toughness of PLA in blend composites or in other niche applications such as cosmetics [53, 54]. PBAT is commonly dissolved in chloroform, which is a toxic halogenated aromatic solvent that has many complications associated with human health. So providing greener and nontoxic solvent options for its processing is pivotal. Anisole is a non-petroleum-based sustainable solvent with a reasonable biodegradation rate [56, 57]. It is a colorless liquid that is typically found in perfumes. It is surprisingly underutilized considering its low toxicity and high sustainability rank in recent classifications [58]. The commercialization of polymer-based electronic devices is further thwarted by the adverse consequences of the hazardous solvents used to manufacture them.

With these insights in mind, this paper aims to take a significant step toward creating sustainable wearable haptic devices. We present a multidisciplinary approach bridging materials science and mechatronics to design the first solar-powered vibrotactile wearable device with biodegradable components and

conductive tracks (see Figure 1) integrated onto a T-shirt. In particular, we present *Eco-Tac*, an eco-friendly and ready-to-use haptic wearable device that provides vibrotactile feedback, incorporates biodegradable components and is connected through degradable conductive tracks to a flexible photovoltaic module that provides solar-based power source to charge the battery of the device. *Eco-Tac* is inspired by our previous device *ErgoTac* [59], which is also a wearable vibrotactile device that has been used in various applications in ergonomics [60, 61], assistance to people with disabilities [62], or robot-human interaction [63]. We show that it is possible to use biobased and biodegradable materials as a component to make a flexible and stretchable biocomposite casing for the vibrotactile device, drastically reducing the amount of non-biodegradable plastic in the device. Data on the manufacturing process and the biocomposite's mechanical properties are reported. The different electronic components of the device are integrated using a new conductive biodegradable ink to simultaneously improve the wearability of the device and its sustainability. This ink allows the integration of the different components onto commercially available cotton T-shirts. Its novel formulation includes anisole as a green solvent, PBAT as a biodegradable binder, and carbon nanofibers providing electrical conductivity. These interconnects are washable with a negligible loss of electrical conductivity. Biological oxygen demand tests are performed to simulate the degradation of such materials in seawater, obtaining a high degradation rate. An experiment with twenty blindfolded subjects performing an assisted manipulation task is conducted to show the potential of such a system in real applications. The results are shown and the outcomes are discussed to highlight the features, benefits, and limitations of the proposed device. In addition, results on the power autonomy of the coupling between an *Eco-Tac* powered by an integrated battery and the commercially available solar panel are reported. The outcomes demonstrate that the device could operate for its entire lifecycle using only solar energy, depending on the environmental conditions. The proposed wearable platform constitutes the first step towards sustainable haptics, and can be used as starting point for the long term vision of building a fully degradable and sustainable wearable vibrotactile device.

## 2 Results and Discussion

The purpose of our T-Shirt is dual, comprising both energy harvesting and its delivery to a wearable device. While the former is achieved through a commercially available solar panel, the connection between this solar panel and the *Eco-Tac* is made of the conductive ink tracks described hereafter. Such tracks can provide an easy integration of the haptic device onto the t-shirt with a high freedom in the design architecture.

### 2.1 Green Conductive Inks and Wearable Interconnects

#### 2.1.1 Materials selection and coating

The conductive inks were made with a green solvent, a biodegradable biopolymer binder, and conductive nanocarbons, as shown in Figure 2. These inks avoided hazardous solvents and privileged carbon nanofibers (CNFs) as conductive nanofiller, a cheap and high aspect ratio carbon-based material [64, 43, 44]. We discover that PBAT biopolymer, dissolved in anisole, has the benefit of easily dispersing for long periods of time (i.e., for 3 days) CNFs without using any surfactant, as shown in Figure S1. The proposed ink is low-cost and could be used with different printing techniques (e.g., spray coating, rod coating, screen printing) depending on the viscosity (i.e., dependent on the ratio between anisole, PBAT, and CNFs). Thus, it is ideal for an industrial scale-up. Additionally, because the chosen biopolymer already possesses mechanical properties necessary for flexible electronics, such as high toughness and elongation at break [65, 66, 67], it does not require the addition of a plasticizing agent [35, 68]. The ink was optimized for spray coating (see the Methods section for more details). We covered a variety of substrates, including paper, cotton, and a polyurethane sponge, as shown in Figure S2. The ink was adhering well to all these surfaces. The ink was coated on a cotton T-shirt (see Figure 2a) for the intended application and on cotton textile for the following characterization.

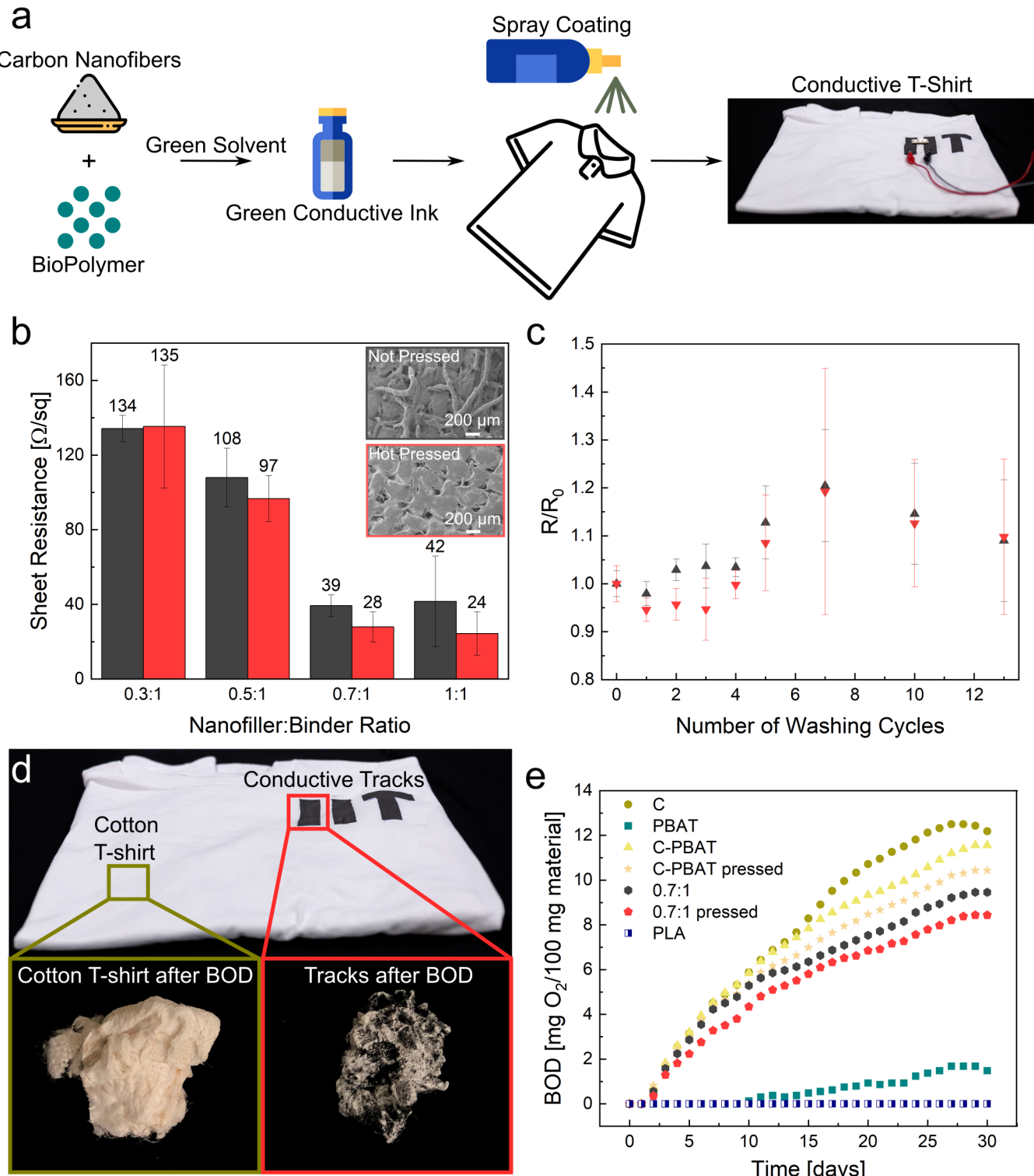


**Figure 2: Green conductive ink deposition and salient features** (a) Scheme of the fabrication of the ink made with the carbon nanofibers and the biopolymer (PBAT) dissolved in anisole and the application on such ink on a cotton t-shirt. (b) Sheet resistance at different nanofiller to biopolymer binder ratio before (black) and after hot pressing (red). (c) Relative resistance  $R/R_0$  against washing cycles, for the 0.7:1 CNF to PBAT ratio without and with the hot-pressing. (d) Photo of the appearance of cotton coated material before and after biological oxygen demand (BOD) biodegradation test in seawater. (e) BOD of the different samples. PLA is reported as a reference. C is the label for the pure cotton sample, C-PBAT and C-PBAT pressed represent the samples with pure PBAT coated on top of cotton before and after hot pressing.

### 2.1.2 Electrical features and micro-texturing

The sheet resistance versus the weight ratio of carbon nanofiber and PBAT loading was determined, as shown in Figure S3 and Figure 2b. The measurements were performed on a sprayed sample before and after hot-pressing since such a procedure can positively influence the coating conductivity, creating a thinner and better-interconnected network of conductive fillers [43], as discussed in the following. The scanning electron microscopy (SEM) micromorphology are presented in Figure S4 and Figure 2b. The hot-pressing procedure was melting the biopolymer but not degrading the materials as confirmed by the differential scanning calorimetry and thermogravimetric analysis of Figure S5 and Figure S6, respectively. The coatings after spray contain a uniform distribution of polymer welded with CNFs. Please note that such procedure did not damage the constituent materials of the coating as shown by the FTIR analysis in Figure S7. In the higher magnification image of Figure S4, a CNFs mat is visible with some pores and a high corrugated surface. These samples have roughness at different scales due to the dimension of the diverse fibers (i.e., a micrometric scale coming from the textile and a nanometric scale due to the CNFs). The cross-sectional images of the not pressed sample in Figure S4 show the conductive layer fluffy and hairy structure, with a thickness of approximately 15-20 micrometers. Upon hot pressing, the coating compactness and adhesion are improved. The ink interacts better with the fabric when hot pressing is used, and it is flattened, closing the open pores on top of the coating, as shown in Figure S4. The coating thickness is reduced to a few micrometers. This factor contributes to decreasing the value of the resistivity, as discussed next.

Regarding the electrical properties, increasing the loading of CNFs, the sheet resistance of samples dropped considerably. A steep decrease of approximately four orders of magnitude occurs between 1:12.5 and 1:10 CNF to biopolymer ratio, as shown in Figure S3. As such, the electrical percolation threshold is in this range of concentration of nanofillers. As seen in Figure 2b, the sheet resistance decreased to around  $30\Omega/\text{sq}$  at 0.7:1 CNF to PBAT ratio, maintaining a similar value at a higher loading. Considering the thicknesses before and after hot-pressing showed in Figure S4, the resistivity of these samples reached values of  $(3.9 \pm 1.2) \times 10 - 2$  and  $(8.4 \pm 2.4) \times 10 - 3 \Omega\text{cm}$ , respectively. Hot pressing significantly reduces the resistivity of the samples. This effect happens for two main reasons: i) hot-pressing lowers the overall sample thickness and ii) it densifies the nanofiller within the PBAT, improving the contact point and, thus, the percolative network. It is worth noting that the achieved sheet resistance and resistivity values are not only comparable but often superior to those reported in prior studies involving coatings with carbon-based nanofillers on cotton. [35] These reported values typically span the range of  $10^8$  to  $10\Omega/\text{sq}$  for sheet resistance and  $10^5$  to  $\times 10^{-3} \Omega\text{cm}$  for resistivity. Importantly, it is essential to emphasize that many of these previous works did not employ environmentally friendly solvents and/or binders in their formulations.

### 2.1.3 Washing stability and mechanical deformation

The following characterization is performed on cotton coated with 0.7:1 CNF to PBAT ratio before and after hot pressing due to the optimal performance they offer in terms of electrical properties and nanofiller loading (see Figure 2b). The washing stability is one of the most critical factors in wearable electronics since it impacts its long-term efficiency. The weak connections between the conductive coating layers and the textile substrate also cause electrical conduction instability and poor durability after repeated washing. Considering this, a test simulating the washing process with detergent was carried in water for half an hour. The impact of the laundry cycles on the relative resistance ( $R/R_0$ ) of the samples is shown in Figure 2c. The as-sprayed and hot-pressed samples increased their initial value or resistance by around 10% after 13 simulated washing machine cycles. Seeing the SEM of the samples after washing (Figure S8), we notice that the morphology is unchanged with this procedure. Using PBAT, which is not dissolved in water and has good adhesion to the substrate, enables such good performance with washing cycles. Moreover, the hydrophobicity of the samples (Figure S9) may also help in reducing the interaction of water during the washing cycles. Other coatings on cotton that used non-biodegradable binders performed worse, doubling the electrical resistance value after similar procedures [69]. As such, we are

## 2.2 Power Autonomy Analysis

confident that our conductive coating can handle routine exposure to pure water and sweat during its operation. Please note that no protective insulating polymeric layer was added on top of the coating, contrary to a strategy commonly seen in literature to ensure washability [51, 70].

Mechanical stresses also play a crucial role in the durability of flexible conductive materials. Thus,  $R/R_0$  is measured before and after folding and pressing with one kg weight at the folding edge. The results are presented in Figure S10. Both samples increase the resistance by around 1.6-1.8 times after ten folding events, a low value compared with similar previous reports [35]. This behavior is due to crack formation during folding. The conductive paths are restored with unfolding since the cracks two edges are in physical contact. The SEM in Figure S10 confirm such a mechanism in the folded and unfolded mode.

### 2.1.4 Degradation in seawater

The biodegradability of the samples was determined by biological oxygen demand (BOD) for 30 days in seawater, a test that can be used to mimic the accidental drop of the material in the ocean [51]. Said test records the oxygen consumption by the microorganisms present in the seawater. Results are reported in Figure 2d and Figure 2e. Figure 2d shows the pure cotton coated with the conductive layer before and after the BOD test. The action of the oxygen consumption by the microorganisms present in the seawater is visible. BOD for the coated samples is shown in Figure 2e. As a reference, we also included the BOD signal of a pristine PLA sample, in which no degradation was detected. It is visible that the pure PBAT starts degrading around the tenth day. This diverse behavior among PBAT and PLA is present because the first is biodegradable while the second is not under the test conditions. The Pure PBAT was tested in the form of a bulk pellet; this may be the reason for the low final BOD of this sample. Indeed, pellets are bulky and not porous; as such, the available surface for the interaction with microorganism is reduced [51]. BOD for the coated samples ranges from 8 to 12 mg O<sub>2</sub> for each 100 mg of material for the 0.7:1 CNF to PBAT pressed sample and pure cotton, respectively. All the samples start to degrade after a couple of days. Differences in maximum values of BOD can be associated with the accessibility, crystallinity, nutritional value, and concentration of the components of the samples [51]. Oxygen consumption is maximum for pure cotton. In this sense, the secreted enzymes by the organisms present in the seawater can more easily access the highly fibrous substrate. The presence of the CNFs reduces the BOD efficiency since they are non-sensitive to the action of the microorganism. Pressing reduces the BOD because a more compact coating layer makes less areas of biodegradable polymer and substrate accessible to microorganisms. Such a mechanism is also microscopically visible: all the samples show a damaged and microporous surface in the SEM after the BOD (Figure S11). The 0.7:1 pressed sample reveals some parts of the coating are relatively low damaged, indicating slower biodegradation probably due to the better adhesion of the coating on the surface and the lower availability of the pure cotton to the microorganism.

## 2.2 Power Autonomy Analysis

To evaluate the capability of our prototype to provide enough energy for an Eco-Tac unit, we measured two values. First, the worst-case discharge time of the Eco-Tac (i.e., the minimal time a device can function solely on its embedded battery). Second, the best-case recharge time (i.e., the minimal time it would take to recharge the device with solar power). Comparing these two values already gives an idea about the system self-sufficiency, however both the power consumption of the Eco-Tac and the power output of the solar panel are highly variable. Estimating the solar cell output power depending on the received light flux is outside the scope of this paper, but we do provide a model of the Eco-Tac current consumption depending on the vibration intensity  $\nu$ .

**Discharge Time.** To estimate the autonomy of the device battery, we monitored the battery voltage with the vibration motor set at maximum intensity, and measured the time it took to go from full charge (circa 4.2 V) to 3.5 V. The battery isn't actually empty at 3.5 V, but getting below a certain level of charge would be detrimental to the battery. The measured discharge time was 2 hours and 44 minutes.

Since the motor vibrating at maximum intensity is far from a realistic use case, we wanted to estimate the autonomy of the device in more practical conditions.

To this end, the current consumption of the device was measured. With the vibration motor turned off, the current drawn from the battery is  $i_{standby} = 7.5 \text{ mA}$ . When the motor is vibrating with intensity  $\nu$ , the total current can be estimated as  $i = 0.62\nu - 70.7 \text{ mA}$  where  $140 \leq \nu \leq 255$  (steady-state). With vibration intensity below 140, the voltage input to the motor would be lower than its minimum operating voltage (see the Methods section for details).

During our manipulation experiment, the mean vibration level of an active Eco-Tac was  $\nu_{mean} = 207$ , and a device was active 20% of the time on average (see Figure 4f). From these data and the aforementioned model, we can determine the maximum current (for  $\nu_{max} = 255$ ) and the mean current:  $i_{max} = 87.4 \text{ mA}$  and  $i_{mean} = 57.6 \text{ mA}$ .

It follows that the ratio of operating mean power consumption during the haptic-guided manipulation experiment (results presented in the next section) versus the maximum power consumption was:  $0.80(i_{standby}/i_{max}) \cdot 0.20(i_{mean}/i_{max}) = 20\%$ . Therefore, in the conditions of the haptic-guided experiment, the device can be expected to work autonomously for about 13 hours and 40 minutes without any recharge.

**Recharge Time.** After discharging the battery to 3.5 V, we recharged it using 2 solar cells in parallel configuration. It took 2 hours and 34 minutes to reach full charge. Naturally, this result depends heavily on lighting conditions. However, since the recharge time was slightly shorter than the discharge time, it shows that in ideal conditions, the 2 solar cells provide slightly more power than what the device is consuming at maximum vibration intensity.

## 2.3 Biocomposite Case Characterization

To improve the sustainability of the Eco-Tac itself, we focused on the main non-commercially available part of the device, which is the case. The amount of silicon used was reduced by mixing it with starch, thus producing a partially biodegradable biocomposite. As a matter of fact, such kind of composites were tested previously to degrade in a few years [71]. The main characteristics of this material are specified here.

### 2.3.1 Morphological analysis of the biocomposite case

In the case of pure silicone, the surface and cross-section appear smooth, as shown in Figure 3a and 3b, respectively. The surface morphology of the biocomposite between biodegradable starch and silicone with which we made the Eco-Tac case is also smooth like silicone (Figure 3c). The SEM micrographs of the cross-section of such composite reveal that the dispersion of starch in the silicone matrix is homogeneous since there is no aggregation of starch particles (Figure 3d). This can be attributed to good compatibility and mixing of silicone and starch.

### 2.3.2 Mechanical properties of the biocomposite case

Figures 3e, 3f and 3g show the results obtained after the tensile tests of different samples developed in this study. Pure silicone shows tensile strength and Young's modulus of  $5.5 \pm 0.5$  and  $8.1 \pm 0.6 \text{ MPa}$ , respectively. Regarding the elongation at break, pure silicone presents a  $144.8 \pm 10.0\%$  value. Adding the 50% biodegradable starch in silicone as fillers, the tensile strength drops to 52.7%, Young's modulus to 46.9%, and elongation at break to 49.4%, respectively. The biocomposite case is flexible, although this drop, with elongation at break of 73.3% and is utilizable satisfactorily in the intended application.

## 2.4 Haptic-guided Manipulation

We investigated the usability of the Eco-Tac in assisting blindfolded people with manipulation tasks. The objective was to reveal its potential for assisting blind individuals in simple activities of daily living,

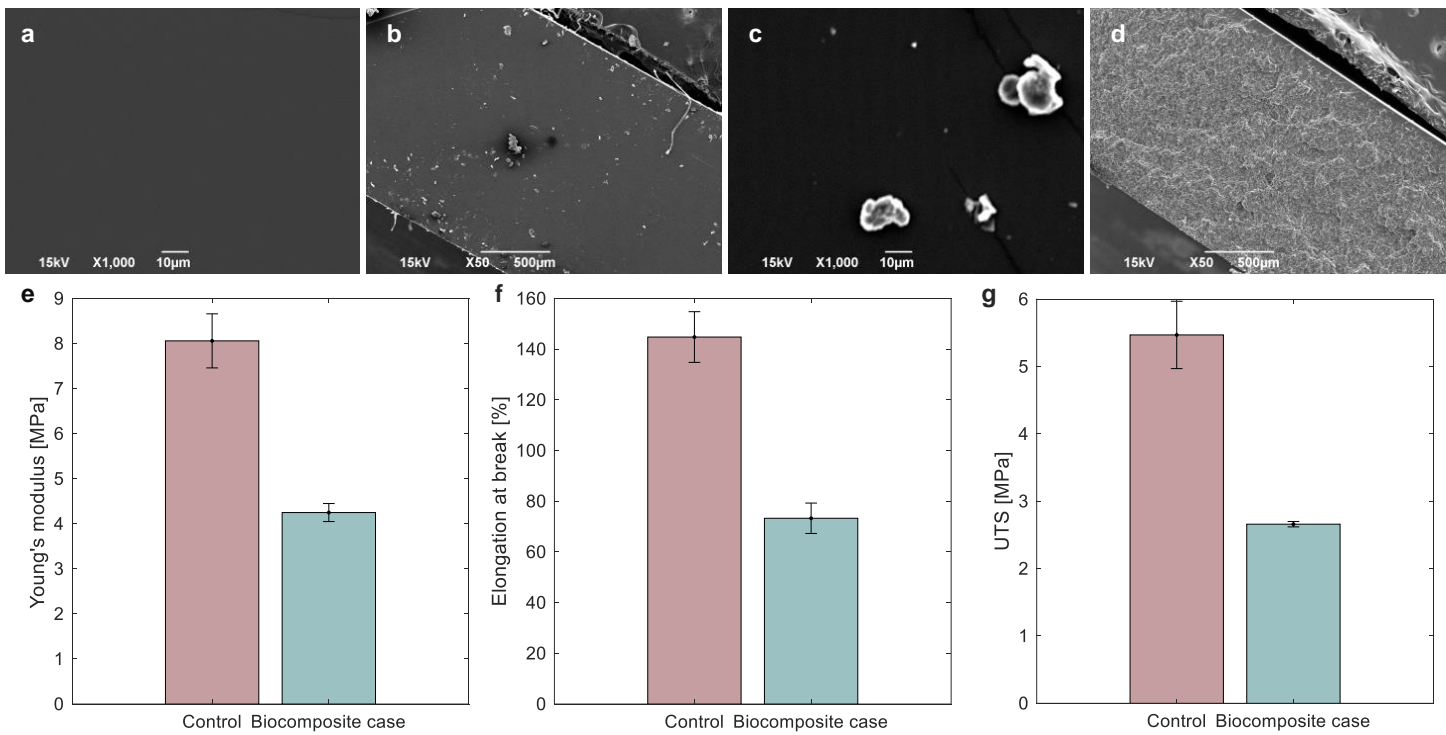


**Figure 3: Biocomposite case characterization results** (a) and (b) SEM images of the morphology and cross-section of the silicone. (c) and (d) surface and cross-section of the biocomposite. (e), (f), and (g) mechanical properties of pure silicon (control, left bar) and biocomposite case (right bar).

by guiding their hands towards certain locations in space. The following section will present the results of the integrated system in this target application.

#### 2.4.1 Experimental setup and protocol

The scenario we chose for this experiment is a path following task, e.g., in pick-and-place activities. Figure 4a shows the experimental setup with the displaced object (a 3D-printed cup) and the user equipment, comprised of four Eco-Tac units and a half-glove with passive markers. The markers were used to track the position of the right hand through an OptiTrack™ motion-capture system to provide feedback to the user based on his/her hand position. The subjects were blindfolded and asked to fetch the cup from the blue box on their right side to bring it on top of the red box on their left side. To this end, they were required to follow a pre-defined path with their right hand, which we call the reference path. Figure 4c depicts the path for the picking phase, while Figure 4d illustrates the path for the placing phase. Neither the initial position of the object nor the paths were known to the subjects beforehand. Furthermore, to avoid nurturing preconceptions about the task, the cup and the boxes were placed on the table only after the subjects were blindfolded.

The positioning of the Eco-Tac units on the user's arm is shown in Figure 4b. Two devices are placed on each side of the right arm, one on the biceps, labeled *U* (Up), one on the triceps, labeled *D* (Down), and two others, labeled *R* (Right) and *L* (Left), respectively on the right and left sides of the forearm. Depending on the position of the user's hand with respect to the reference path, one of these devices is activated. The *R* and *L* devices are guiding the user along the horizontal direction (x-axis), while the arm devices are guiding him up or down (y-axis). For details about the feedback direction selection, refer to the Methods section.

Complementing the directional feedback aforementioned, a signal was triggered when the user's hand was detected within range of picking the cup, as well as in the final position. This signal was composed of all four Eco-Tac devices vibrating conjointly and was interpreted by the user as a cue to either grasp or release the cup depending on the situation.

Before attempting the actual task, the subjects underwent a training phase in which they were asked to

follow a partially known path. They were told the general directions of the training path (up, then left) and encouraged to experiment with the system, so as to get familiar with how the feedback is given.

#### 2.4.2 Feedback generation

To generate vibrotactile feedback from a reference path, we render a virtual environment encompassing the predefined path for the user's right hand and a set of virtual walls around it, as shown in Figure 4c and 4d. As soon as the user's hand crosses one of the walls, getting away from the path, a vibrotactile stimulus is provided through an Eco-Tac. Indeed, the feedback is given in the form of repulsive cues, with the Eco-Tac devices driving the user back toward the reference path. Figure 4b shows which device vibrates depending on the direction in which the user should move. Besides, the vibrations get stronger as the user's hand moves further away from the reference path. We choose this approach (i.e., not to give any feedback while the user is moving on the right track, rather than providing cues about the direction to take) to minimize the amount of time when a device is activated, because an increase in user discomfort has been reported with increasing duration of the vibration [72].

In Figure 4b, the computation of the feedback intensity is illustrated. Let us define  $\hat{\mathbf{p}} \in \mathbb{R}^2 = [\hat{x}, \hat{y}]$  as the reference point towards which the user is guided, and  $\mathbf{p} \in \mathbb{R}^2 = [x, y]$  as the user's right hand position, considering the human coronal plane as the x-y plane. The errors  $\varepsilon_x$  and  $\varepsilon_y$  between  $\hat{\mathbf{p}}$  and  $\mathbf{p}$  are computed as:

$$\begin{cases} \varepsilon_x = \hat{x} - x \\ \varepsilon_y = \hat{y} - y. \end{cases} \quad (1)$$

The vibration intensity  $\nu$  of the Eco-Tac is computed as a function of  $\varepsilon$ , where  $\varepsilon$  is equal to either  $\varepsilon_x$  or  $\varepsilon_y$  depending on the feedback direction.

$$\begin{cases} \nu = 0 & \text{if } |\varepsilon| < \varepsilon^{\text{th}} \\ \nu = (|\varepsilon| - \varepsilon^{\text{th}}) \frac{\nu^{\max} - \nu^{\text{th}}}{\varepsilon^{\text{sat}} - \varepsilon^{\text{th}}} + \nu^{\text{th}} & \text{if } \varepsilon^{\text{th}} \leq |\varepsilon| \leq \varepsilon^{\text{sat}} \\ \nu = \nu^{\max} & \text{if } |\varepsilon| > \varepsilon^{\text{sat}} \end{cases} \quad (2)$$

where  $\varepsilon^{\text{th}}$  is the error threshold beyond which the Eco-Tac is activated,  $\nu^{\text{th}}$  is the vibration intensity at the latter threshold,  $\varepsilon^{\text{sat}}$  is the saturation error (i.e., the error that we expect to be the highest), and  $\nu^{\max}$  is the maximum vibration intensity. In brief,  $\varepsilon^{\text{th}}$  represents the distance between the virtual walls; beyond the walls, the vibration intensity is proportional to the error  $\varepsilon$  until the maximum vibration intensity  $\nu^{\max}$  is reached at  $\varepsilon^{\text{sat}}$ , and is kept constant above.

During the experiment, the activation threshold was set at  $\varepsilon^{\text{th}} = 4$  cm, and the saturation error at  $\varepsilon^{\text{sat}} = 20$  cm. Additional information about the guidance strategy is provided in the Methods section, along with the algorithm implemented.

#### 2.4.3 Experimental findings

Figures 4e and 4f show how subjects performed the experiment using our guidance system. Figure 4e illustrates, for one average subject as an example, the measured hand position  $\mathbf{p}$  with respect to the reference point  $\hat{\mathbf{p}}$  over time, considering the  $x$  and  $y$  coordinate separately (upper left and right graphs, respectively), and the vibration intensities of the corresponding Eco-Tac devices,  $L$  and  $R$  for the  $x$ -coordinate and  $U$  and  $D$  for the  $y$ -coordinate (lower left and right graphs, respectively). The subject was able to successfully execute the task with few instances of a device reaching the saturation point.

The boxplots in Figure 4f show some statistical results for all the recruited subjects instead. We defined the activation ratio  $r_A$  as the ratio between an Eco-Tac active time (i.e. time during which an Eco-Tac is vibrating) and total time. The average activation ratio and the average intensity level  $\nu$  among all subjects are presented for each device (left upper and lower graphs, respectively). The average activation ratio is higher for the  $L$  and  $D$  devices, likely due to the shape of the reference path. The differences between average intensity levels can be linked to differences in the sensitivity of the various parts of the

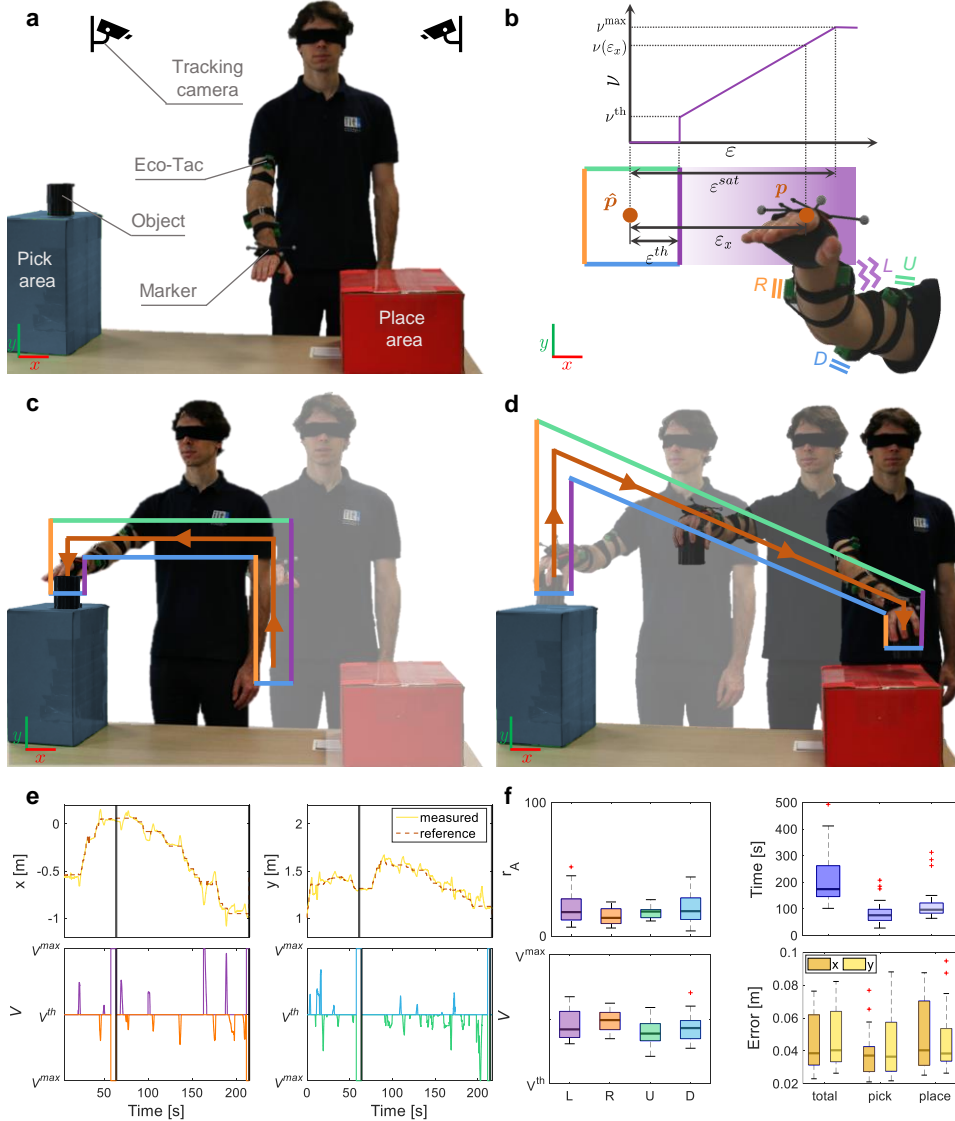


**Figure 4: Haptic-guided manipulation experiment** (a) Experimental setup. (b) Graphical representation of the vibration intensity depending on the error amplitude, and illustration of the activated device depending on the error direction. (c) Reference path for the picking phase. (d) Reference path for the placing phase. (e) Results of a single subject: Reference tracking (top) and devices feedback (bottom). (f) Statistical results of all subjects: activation ratio and vibration intensity of each device (left), task completion time and tracking error (right).

arm where the devices are placed. The average completion time and the average errors  $\varepsilon$  among all subjects are presented for the total task, the picking phase, and the placing phase (right upper and lower graphs, respectively). Apart from a few outliers, most subjects were able to complete the task within 5 minutes, and to follow the path with an average error lower than 7 cm. The diagonal part of the second phase proved to be slightly harder to follow than straight lines, as can be seen from the longer completion time and higher average errors compared to the first phase.

In addition, the correlation was computed between the total task completion time and the training time for all the subjects, and the hypothesis of no correlation was tested with a confidence level equal to 0.05. A positive value equal to 0.6781 was found with a p-value equal to 0.001, meaning that the training and the completion time have a significant positive correlation. From this result, we can infer that some people find the use of the system more intuitive than others, and that the short training phase is not sufficient to even out those differences. We could expect faster and more consistent task completion times from users more familiar with the system.

### 3 Conclusion

In this article, we presented Eco-Tac, an ECO-friendly vibroTACtile device, with a potential application in manipulation guidance for visually impaired people. In more details, the following contributions were presented: *i*) description of the *Eco-Tac* device, as a novel, eco-friendly and ready-to-use haptic wearable device that provides vibrotactile feedback, incorporating biodegradable components as well as a solar-based power source to guide visually impaired people in manipulation tasks. The device is integrated onto a cotton T-shirt. *ii*) a new conductive and biodegradable ink with a novel formulation that allows integration of all the different components (i.e., the power source and the vibrotactile device) onto the T-shirt. The formulation includes anisole, a green solvent, and PBAT, a biodegradable biopolymer binder already large-scale produced together with carbon nanofibers providing electrical conductivity. The deposition procedure is spray coating, a simple and industrially-compatible coating method already heavily used in many essential industries, e.g., automotive. *iii*) the use of biobased and biodegradable materials to make the casing of the device, reducing drastically the amount of non-biodegradable plastic. *iv*) an experimental evaluation with 20 blindfolded subjects performing an assisted-manipulation task. This work is highly interdisciplinary, bridging materials science and mechatronics, and was realized considering the United Nations' Sustainable Development Goals (SDGs) as pivotal for robotics and electronics in general. Indeed the power is obtained from renewable sources (SDG 7, Affordable and Clean Energy), and ad-hoc materials (i.e., the conductive ink/track, and the biocomposite case) were designed to reduce the environmental impact of the final device (SDG 12, Responsible Production and Consumption) in terms of *e*-waste generated. In particular, the Eco-Tac case was made with a biocomposite that can degrade in a timescale of a few years [71] if unintentionally discarded in the environment. One important application area of the Eco-Tac is industry, where it could improve people's working conditions, in particular through ergonomics feedback and human-robot interaction [59] (SDG 9, Industry, Innovation, Infrastructure). Since workers' outfits are usually custom-made, the integration of the Eco-Tac and printed wiring can be easily achieved. Even though the prototype T-shirt we made connects a single solar panel to a single vibrotactile unit, it is a proof of concept that demonstrates the feasibility of an outfit integrating multiple devices and power sources, as well as other types of wearables (e.g. health monitoring sensors). The presented work promotes the use of sustainable materials, power sources, and methods in integrated wearable systems.

While the electronic architecture of the Eco-Tac (further detailed in the Methods section) was chosen with versatility in mind, allowing us to use the devices in diverse configurations, it is not optimized for any particular application. Currently, each device has its own battery and power management circuitry. In case the number of devices were set in advance, a more efficient solution would be to rely on a single centralized battery and power management system, which could dispatch power to the different devices. This would reduce the overall power consumption of the system, since a single battery load management unit and a single voltage regulator would be required, instead of one per device. Besides, externalizing

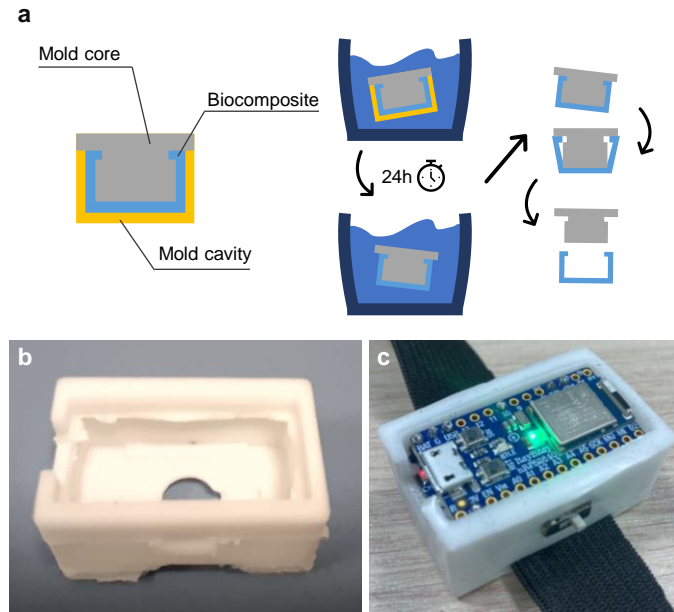


**Figure 5: Schematic representation of the fabrication process of the biocomposite case where (a) illustrates the molding process, (b) the molded case, and (c) is the final Eco-Tac device including the case and the embedded electronic components.**

the battery and designing a custom PCB would permit a significant reduction in size of the device. Finally, since the batteries are usually the first elements to wear out, having a single, easily replaceable battery would make for a more sustainable approach. Further improvements will include a fully biobased and biodegradable case that can degrade quickly after the appropriate stimuli (e.g., water immersion, change in pH, temperature) is provided. The conductive tracks will also be fully degradable, taking advantage of strategies used for transient devices [73, 74, 75, 76]. Structural electronics parts, such as printed circuit boards, will also be customized towards biodegradability to complement the biodegradable case.

## 4 Methods Section

### 4.1 Manufacturing processes

#### 4.1.1 Biocomposite case

The polydimethylsiloxane elastomeric silicone materials, Sylgard 184, two-part (10 to 1 mix ratio), viscosity cP 5100, and working time at 25°C (Pot Life – 1.5 hours) was obtained from the Dow Chemical Company, USA. Cornstarch was obtained from Merck Life Science S.r.l., Milan, Italy. To remove the moisture, first, the cornstarch was dried at 60°C in an oven for 8 h and then cooled it at room temperature (RT) for 2 h. The dried starch powder (50% by weight) was then manually mixed with 50% silicone without adding any solvent. The mixing process was continued for 10-15 minutes to get homogeneous dispersion of starch in silicone. The mixer was then put in a vacuum chamber at 1 bar for 15 min to degas the trapped air. Both the mold core and the mold cavity were manufactured with an additive process. The mold core was made with aluminum, and the mold cavity was made with 3D printable polyvinyl alcohol (PVA) filament. Once the silicone/starch mixed solution was poured into the mold, the mold cavity was covered with the mold core and cured at room temperature for 24 hours. The mold cavity was then dissolved in water within 24h, so the molded object could easily be retrieved. A schematic of the process is shown in Figure 5. Note that the same mold can be used several times to manufacture the biocomposite case.

#### 4.1.2 Biodegradable conductive ink

Anisole and graphitized CNFs (grade PR-25-XT-HHT from Pyrograf Products Inc., nominal length between 20 and 200 $\mu\text{m}$ , diameter  $\approx 100\text{nm}$ )<sup>(1)</sup> were purchased from Sigma-Aldrich. PBAT was obtained from Xinjiang Blue Ridge Tunhe Polyester Co., Ltd (grade TH801T, melting at 110 – 120°C, tensile strength 25MPa, elongation at break > 500%, Mw  $\approx 7.5 \cdot 10^4\text{gmol}^{-1}$  [66, 67]. The bio-based ink for spray coating is made up of only the previously mentioned three components through some straightforward steps. First, one weight % PBAT was dissolved in anisole. To speed up the dissolution of PBAT into anisole, the vial containing the ingredients can be heated up with a hot plate at 70°C under stirring. Eventually, the PBAT concentration can be augmented if another technique needing higher viscosity materials (e.g., such as screen printing or 3D printing) is used. Afterward, the desired amount of CNFs was added directly to the polymeric solution and was probe sonicated for 3 minutes. The ratio between the PBAT and CNFs was changed from CNF:PBAT 0.01:1 to 1:1. Typically, 10ml of the ink was spray coated on a cotton fabric substrate of 35cm<sup>2</sup>. The optimal spray parameter is 2.0bar, 15 – 20cm distance. The spray used is a VL siphon from Paasche. While spraying, a heat gun was heating up the target surface at a temperature of 120-150°C to ensure the solvent evaporation and enhance the adhesion. This specific procedure was carefully designed to ensure the complete evaporation of anisole, and, at the same time, was enhancing the adhesion of the coating on the sprayed substrates. Indeed, the PBAT binder's melting temperature (around 120°C, as evidenced by the DSC data in Figure S5) is reached, while the degradation temperature, far higher than 200°C, was not (see TGA of Figure S6). After spray, a hot-pressing procedure was performed on selected samples at 120°C under 9.3kPa for 10 minutes, using a Carver press (model 3853CE).

## 4.2 Materials characterization protocols

All the measurements regarding the inks and the case material were taken on minimum three samples unless specified differently.

SEM was performed using a JEOL JSM-6490 L at 10kV collecting secondary electrons. Prior to imaging, a layer of gold with a thickness of  $\sim 10\text{nm}$  was sputtered on the samples surfaces using a Cressington 208 HR sputter coater to improve sample conductivity. For cross-sectional SEM imaging, the samples were cooled using liquid nitrogen and then fractured. TGA of the specimens was done by means of a TA instruments machine (model Q500) in N2 flow, increasing the temperature till 800°C.

Differential scanning calorimetry was performed with a TA-Instruments Discovery DSC 250 in the range –70 – 200 °C, while heating the samples at 10 °C/min in N2 atmosphere. The I–V curves were measured by means of a source-meter from Keithley (model 2450) in the four-probe arrangement. Silver paste (RS pro, product number 186–3600) was painted, forming 5mm wide contacts (W) spaced by 5mm (L) on rectangular shaped specimens on glass slides. The thickness of the samples was measured with cross sectional SEM images and was of  $\approx 15\mu\text{m}$  for the sprayed sample and  $\approx 3\mu\text{m}$  for the hot-pressed ones. The electrical resistance (R) of the coatings was then extracted from the I-V curved and the resistivity ( $\rho$ ) was then calculated considering the described geometry through the equation:

$$\rho = R \frac{Wt}{L}. \quad (3)$$

The test simulating the washing process was carried out using roughly 5.0g/L of detergent in 0.5l of water for half an hour. The samples were placed under stirring at a temperature of 50°C. After washing, all the samples were given an additional rinsing in water under the same conditions for a total of two times. The impact of the laundry cycles on the relative resistivity ( $R/R_0$ ) of the samples is measured with the Keithley.

The folding stability of the electrical features after repeated fold–unfold cycles was recorded measuring  $R/R_0$  in the direction perpendicular to the folding edge. A weight of  $\approx 1\text{kg}$  was placed on the fold mark during the folding event.

Static water contact angles of the pastes were measured by an optical contact angle device (DataPhysics).

Ten microliters of deionized water were deposited on the samples. Five specimens were tested for each sample and the mean value with the standard deviation was reported.

Biodegradability was assessed by measuring the biochemical oxygen demand (BOD) with the OxiTop-IDS system. It was determined by monitoring the oxygen consumption in a closed bottle filled with 432ml of seawater as the single carbon source and 200mg of each sample. In particular, seawater was chosen in order to mimic real environmental conditions. Indeed, it contains microorganisms and nutrients needed for their growth. The experiments were conducted at RT inside dark glass bottles hermetically closed with the OxiTop measuring head. Sodium hydroxide was used as a  $CO_2$  scavenger to sequestrate carbon dioxide produced during biodegradation, and biotic consumption of the oxygen present in the free volume of the system was measured as a function of the decrease in pressure. Raw data of oxygen consumption ( $mgO_2/l$ ) were corrected by subtracting the mean values of the blanks obtained by measuring the oxygen consumption of the seawater in the absence of any test material. After this subtraction, values were normalized on the mass of the individual samples and referred to 100 mg of the material ( $mgO_2/100mg$ ).

The tensile testing measurements were conducted with an Instron dual column tabletop universal testing system (Model 3365L4052) with a 2kN load cell, following the ASTM D638 standard test methods for tensile properties of plastics and other resin materials at 25°C. Specimens of about 1.2 mm thickness were first conditioned for 48h at standard laboratory conditions (i.e.,  $21 \pm 2^\circ C$  and  $50 \pm 2\% RH$ ). Then, they were cut with a dog bone press (length of 35mm, width of 4mm) and were tested at a rate of 10mm/min. From the obtained stress-strain curves, Young's modulus, ultimate tensile strength, and elongation at break were calculated. For each sample, five specimens were tested, and for each parameter, the mean value with the standard deviation was reported.

## 4.3 Hardware Description

### 4.3.1 Eco-Tac vibrotactile device

Eco-Tac is a redesigned version of the ErgoTac presented in [59]. The base concept is a wearable device, connectable via Bluetooth Low Energy (BLE), which can transmit information to its user through vibrations.

Compared to the ErgoTac, the Eco-Tac version is smaller ( $41 \times 25 \times 17.7$  mm), more comfortable to wear thanks to the use of a flexible biocomposite for the case, and features a slightly more powerful actuator. Besides, the actuator is now placed in a hole within the bottom side of the case, thus being in direct contact to the user's skin or clothes, and improving the sensation of low intensity vibrations.

The electronics are described in Figure 6a and are based on 3 boards from Adafruit. The ItsyBitsy nRF52840 Express board (Figure 6a, 1) hosts the main processing unit, a Nordic nRF52840 Bluetooth LE chip. It features a 64 MHz CortexM4 processor, and a 2,4 GHz radio module compliant with Bluetooth Low Energy (BLE) specifications. The boards further includes a voltage regulator and a microUSB connector for programming and recharging the device. The motor is controlled through the DRV2605L Haptic Driver from Texas Instruments, mounted on a second Adafruit breakout board (Figure 6a, 3). The motor itself is an eccentric rotating mass from Precision Microdrive (model number 310-118), 10 mm in diameter and 2 mm in thickness (Figure 6a, 6). For managing the battery charge, we use the Adafruit LiIon/LiPoly backpack board (Figure 6a, 2), which is based on the MCP73831 from Microchip. The battery is a 3.7 V, 250 mAh Lithium-Ion from Jauch (Figure 6a, 5). A tiny slide switch (SSSS213000 from Alps Alpine, Figure 6a, 4) is used as power switch.

To attach the case to the user's body, a strap is used. This strap can be easily tightened thanks to a small, custom-designed, sintered buckle. The material used for the latter is the DuraForm ProX PA. Detailed instructions on how to assemble the Eco-Tac are provided in the supplementary materials.

### 4.3.2 Functionalized T-Shirt

Two versions of the T-Shirt were made. One has the solar panel glued to it, the other relies on conductive hook & loop tape to fasten the solar panel onto the T-Shirt. This makes it easy to remove the solar

cell, and thus to wash the T-Shirt.

**Solar panels.** The solar panels selected are the PowerFilm MPT4.8-150. Those are thin, flexible cells, of  $94 \times 73$  mm, rated to deliver 480 mW. In practice, the power output is extremely dependent of lighting conditions. A more detailed characterization of these cells would be out of the scope of this paper.

**System Integration.** Eco-Tac being recharged through a microUSB connector, we glued wires to the conductive tracks to connect the device to them. The CW2400 from Chemtronics, a conductive epoxy glue, was used for this. In the glued version, the solar panel was connected to the other end of the tracks with that same glue, and was attached to the T-Shirt with the Super 77 spray adhesive from 3M. In the hook & loop tape version, the tape bands were stitched to the T-Shirt and connected to the tracks with the CW2400 glue. The same glue was used to connect the solar cell to the matching part of the tape.

## 4.4 Firmware Description

### 4.4.1 Embedded program

The vibration intensity is controlled by an 8-bits value  $\nu$  transmitted via BLE. The microcontroller is programmed to keep vibrating at the same intensity until this value is overwritten. When 0 is received, the motor driver goes into sleep mode. The only vibration type we used for the experiment described above is a continuous vibration. In continuous mode,  $\nu$  is interpreted as a duty cycle value, so the average voltage input of the motor is proportional to  $\nu$ . When  $\nu < 140$ , the mean voltage is lower than 1.8 V, which is the minimum operating voltage of the motor. Therefore, the range of  $\nu$  is [140; 255] in continuous mode.

Though we didn't use this feature for our haptic guidance experiment, it is possible to use the values between 1 and 139 for other vibration types. As an example, we encoded specific vibration patterns, including a heartbeat-like signal, from specific values of  $\nu$ . This discrete mode makes use of the haptic waveform library included in the DRV2605L driver.

### 4.4.2 Computer Interface

The software architecture is depicted in Figure 6b. The program interfacing the Eco-Tac devices with the host computer is comprised of two ROS nodes. The first one is a BLE interface, which passes the transaction data to the Bluetooth driver. This transaction data includes the address of the device, the GATT characteristic to use, and the value to write. The second node converts higher level data, namely an Eco-Tac device ID and a vibration intensity value, into the aforementioned Bluetooth transaction data.

## 4.5 Vibrotactile Guidance for Blind Manipulation

In this section, the guidance strategy implemented to assist blind people during manipulation tasks with vibrotactile feedback is illustrated in detail. In addition to how the feedback intensity is computed, which was already mentioned in the *Feedback generation* section, two other important parts of the method are the computation of the point towards which the user is guided on the one hand, and the selection of the feedback direction on the other hand.

### 4.5.1 Reference Point Update

Let us consider the reference path  $P$  as a set of reference points  $\hat{\mathbf{p}}$ . We define  $\mathbf{p}_k$  as the position of the user's hand at iteration  $k$ , and  $\hat{\mathbf{p}}_k$  as the reference point of  $P$  towards which the user is guided at the same iteration  $k$ . We call the latter the target reference point. Finally we define  $\hat{P}_k$  as a subset of  $P$  containing the reference points comprised between the target reference point  $\hat{\mathbf{p}}_k$  and the end of the path. All those elements are shown in Figure 6c.

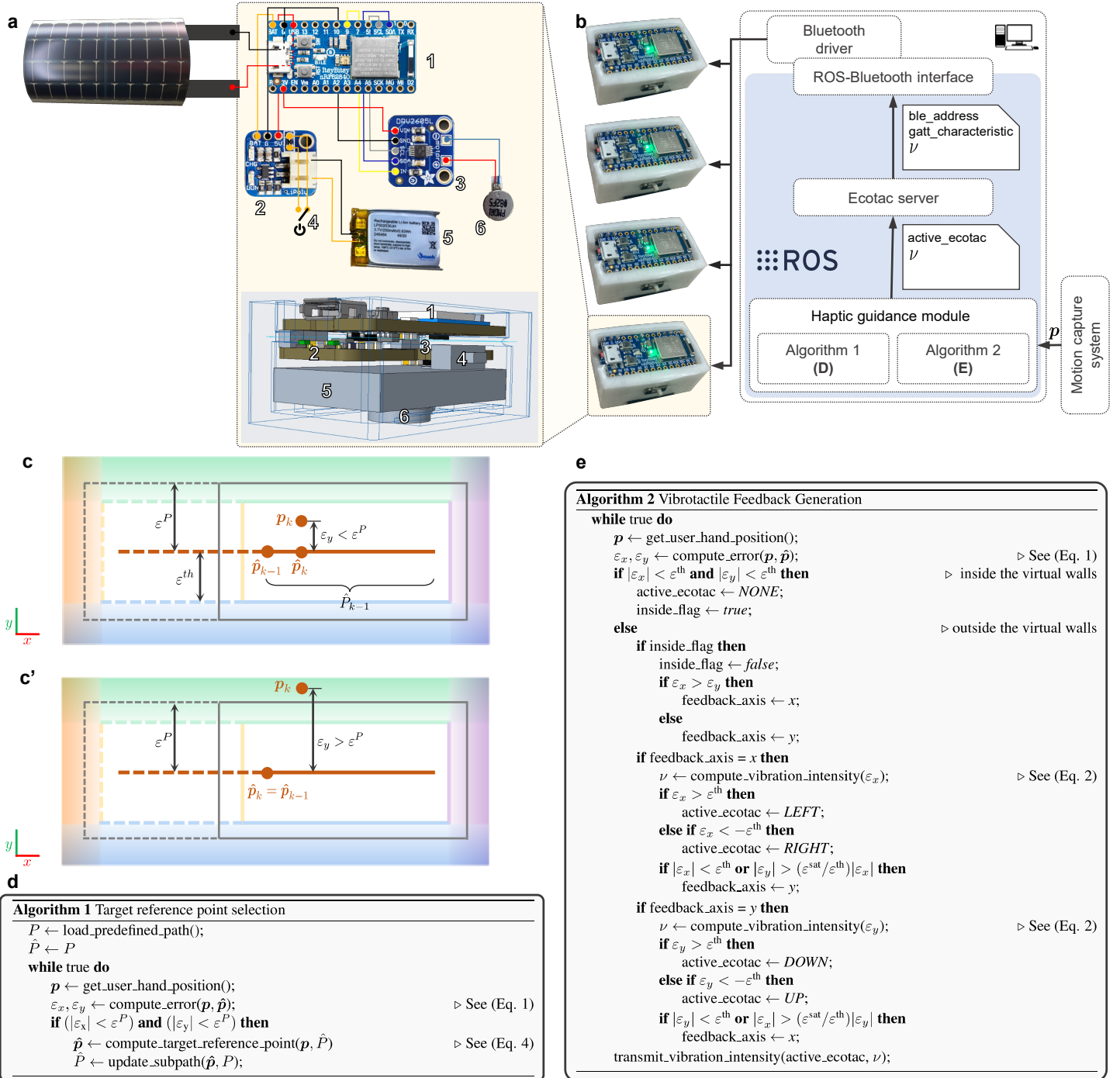


Figure 6: **Schematics of the proposed device and detailed methodology** (a) Hardware components of the Eco-Tac. (b) Haptic guidance system software architecture and communication workflow. (c) Illustration of the target reference point update. (c') Example case of the target reference point not being updated (d) Target reference point selection algorithm (e) Vibrotactile feedback generation algorithm.

The target reference point is updated only when both the errors  $\varepsilon_x$  and  $\varepsilon_y$  defined in (Eq. 1) are below a threshold  $\varepsilon^P$ . When this condition is fulfilled, the target reference point  $\hat{\mathbf{p}}_k$  is the point of  $\hat{P}_k$  which is the closest to  $\mathbf{p}_k$ , and can be computed as:

$$\hat{\mathbf{p}}_k = \arg \min_{\hat{\mathbf{p}} \in \hat{P}_k} d(\hat{\mathbf{p}}, \mathbf{p}_k) = \{\hat{\mathbf{p}} \mid \forall \hat{\mathbf{q}} \in \hat{P}_k : d(\hat{\mathbf{q}}, \mathbf{p}_k) \geq d(\hat{\mathbf{p}}, \mathbf{p}_k)\} \quad (4)$$

where  $d(\hat{\mathbf{p}}, \mathbf{p}_k)$  is the distance between any reference point  $\hat{\mathbf{p}} \in P$  and the current user's hand position  $\mathbf{p}_k$  equal to:

$$d(\hat{\mathbf{p}}, \mathbf{p}_k) = \sqrt{(\hat{x} - x_k)^2 + (\hat{y} - y_k)^2}. \quad (5)$$

When the target reference point is updated, so is the subpath  $\hat{P}_k$ , by removing from it the reference points that have been passed by. In other words, once the user has passed a reference point, she/he cannot be guided towards this point anymore. This ensures that the path can only be followed forward.

When either  $\varepsilon_x$  or  $\varepsilon_y$  goes above  $\varepsilon^P$ , the target reference point is fixed at the point where the user left the path, as illustrated in Figure 6c'. The selection of the target reference point  $\hat{\mathbf{p}}_k$  is summarized with the pseudocode in Figure 6d.

$\varepsilon^P$  represents the tolerance within which the user can be considered to follow the path. The need to set a lower error threshold ( $\varepsilon^{\text{th}}$ ) to trigger the feedback naturally arises from the fact that the user cannot be expected to follow the path without ever triggering the feedback from the system. In other words, we implement a buffer zone between  $\varepsilon^{\text{th}}$  and  $\varepsilon^P$ , where the user is still in an admissible position but already receives feedback directing him back towards the reference path.

During the experiments, the reference update threshold was set at  $\varepsilon^P = 1.5\varepsilon^{\text{th}} = 6\text{cm}$ .

#### 4.5.2 Feedback direction selection

Here we explain how we select the direction of the feedback. As a matter of fact, it is likely that both  $\varepsilon_x$  and  $\varepsilon_y$  will be above  $\varepsilon^{\text{th}}$  at the same time. However, it has been demonstrated that the stimuli localization accuracy decreases with the increase in the number of activated cues [77, 78]. Therefore, our implementation only transmits feedback from one Eco-Tac at a time to maximize the user capacity to distinguish signals coming from different devices and thus different guidance directions.

At the first iteration after the user moved out of the virtual walls, the direction with the highest error is selected as feedback direction. Then, the feedback direction should remain the same until the error along this direction gets corrected. This ensures that the system will not switch back and forth from one direction to the other, which would be confusing for the user. This being said, some users may not perceive low-intensity vibrations, and therefore may not feel any feedback when the error in the feedback direction is too low. In such a case, if the user starts moving perpendicularly to the feedback direction, she/he could get far away from the path while maintaining a low error in the feedback direction (despite the high error in the other direction), thus not perceiving any feedback and believing to be on the right path.

To mitigate this issue, a condition to switch direction was added. If the error ratio (either  $\varepsilon_x/\varepsilon_y$  or  $\varepsilon_y/\varepsilon_x$ ) becomes higher than the ratio between  $\varepsilon^{\text{sat}}$  and  $\varepsilon^{\text{th}}$ , the feedback direction becomes the one with the highest error. The feedback direction selection and intensity calculation are brought together in the algorithm of Figure 6e.

#### Supporting Information

Supporting Information is available from the Wiley Online Library or from the author.

#### Acknowledgements

The authors acknowledge Lara Marini for the help with the TGA and DSC measurements, Claudio Semini for suggesting the use of conductive hook & loop tape, and Pinar Sencandan for her help with stitching tasks. This work is part of the Sustainability Initiative of IIT.

**Funding** This work was supported in part by the ERC-StG Ergo-Lean (Grant No.850932). PC acknowledges funding from the Marie Skłodowska-Curie actions (project name: BioConTact, Grant Agreement No. 101022279) under the European Union's Horizon 2020 research and innovation programme.

## References

- [1] A. Ajoudani, A. M. Zanchettin, S. Ivaldi, A. Albu-Schäffer, K. Kosuge, O. Khatib, *Autonomous Robots* **2018**, *42*, 5 957.
- [2] O. Yasa, Y. Toshimitsu, M. Y. Michelis, L. S. Jones, M. Filippi, T. Buchner, R. K. Katzschmann, *Annual Review of Control, Robotics, and Autonomous Systems* **2022**, *6*.
- [3] Amisha, P. Malik, M. Pathania, V. K. Rathaur, *Journal of Family Medicine and Primary Care* **2019**, *8*, 7 2328.
- [4] D. Minh, H. X. Wang, Y. F. Li, T. N. Nguyen, *Artificial Intelligence Review* **2022**, 1–66.
- [5] I. Ahmed, G. Jeon, F. Piccialli, *IEEE Transactions on Industrial Informatics* **2022**, *18*, 8 5031.
- [6] R. Rautela, S. Arya, S. Vishwakarma, J. Lee, K.-H. Kim, S. Kumar, *Science of the Total Environment* **2021**, *773* 145623.
- [7] F. Hartmann, M. Baumgartner, M. Kaltenbrunner, *Advanced Materials* **2021**, *33*, 19 2004413.
- [8] M. Irimia-Vladu, *Chem. Soc. Rev.* **2014**, *43* 588.
- [9] G. Cantarella, M. Madagalam, I. Merino, C. Ebner, M. Ciocca, A. Polo, P. Ibba, P. Bettotti, A. Mukhtar, B. Shkodra, A. S. Inam, A. J. Johnson, A. Pouryazdan, M. Paganini, R. Tiziani, T. Mimmo, S. Cesco, N. Münzenrieder, L. Petti, N. Cohen, P. Lugli, *Advanced Functional Materials* **2023**, 2210422.
- [10] E. H. Rumley, D. Preninger, A. S. Shomron, P. Rothmund, F. Hartmann, M. Baumgartner, N. Kellaris, A. Stojanovic, Z. Yoder, B. Karrer, C. Keplinger, M. Kaltenbrunner, *Science Advances* **2023**, *9*, 12 eadf5551.
- [11] S. C. Mukhopadhyay, *IEEE Sensors Journal* **2014**, *15*, 3 1321.
- [12] S. Gong, W. Schwallb, Y. Wang, Y. Chen, Y. Tang, J. Si, B. Shirinzadeh, W. Cheng, *Nature communications* **2014**, *5*, 1 3132.
- [13] M. H. Iqbal, A. Aydin, O. Brunckhorst, P. Dasgupta, K. Ahmed, *Journal of the Royal Society of Medicine* **2016**, *109*, 10 372.
- [14] J. Wang, S. Li, F. Yi, Y. Zi, J. Lin, X. Wang, Y. Xu, Z. L. Wang, *Nature communications* **2016**, *7*, 1 12744.
- [15] T. R. Ray, J. Choi, A. J. Bandodkar, S. Krishnan, P. Gutruf, L. Tian, R. Ghaffari, J. A. Rogers, *Chemical Reviews* **2019**, *119*, 8 5461.
- [16] S. Zhang, Y. Zhou, A. Libanori, Y. Deng, M. Liu, M. Zhou, H. Qu, X. Zhao, P. Zheng, Y.-L. Zhu, et al., *Nature Electronics* **2023**, 1–11.
- [17] H. A. Sonar, J.-L. Huang, J. Paik, *Advanced Intelligent Systems* **2021**, *3*, 3 2000168.
- [18] S. Scheggi, A. Talarico, D. Prattichizzo, In *22nd Mediterranean Conference on Control and Automation*. **2014** 20–23.
- [19] Q. Hua, J. Sun, H. Liu, R. Bao, R. Yu, J. Zhai, C. Pan, Z. L. Wang, *Nature communications* **2018**, *9*, 1 244.
- [20] K. Kim, J. E. Colgate, *IEEE Transactions on Neural Systems and Rehabilitation Engineering* **2012**, *20*, 6 798.
- [21] P. B. Shull, D. D. Damian, *Journal of Neuroengineering and Rehabilitation* **2015**, *12* 1.

- [22] S. Fani, S. Ciotti, M. G. Catalano, G. Grioli, A. Tognetti, G. Valenza, A. Ajoudani, M. Bianchi, *IEEE Robotics & Automation Magazine* **2018**, *25*, 1 77.
- [23] Z. Sun, M. Zhu, X. Shan, C. Lee, *Nature Communications* **2022**, *13*, 1 5224.
- [24] K. R. Sheerin, D. Reid, D. Taylor, T. F. Besier, *Physical Therapy in Sport* **2020**, *43* 173.
- [25] M. F. Jimenez, R. C. Mello, T. Bastos, A. Frizera, *Medical Engineering & Physics* **2020**, *80* 18.
- [26] T. Stegmaier, *The Global Textile and Clothing Industry* **2012**, 113–130.
- [27] A. Lund, Y. Wu, B. Fenech-Salerno, F. Torrisi, T. B. Carmichael, C. Müller, *MRS Bulletin* **2021**, *46*, 6 491.
- [28] Y. Tang, B. Guo, M. A. Cruz, H. Chen, Q. Zhou, Z. Lin, F. Xu, F. Xu, X. Chen, D. Cai, B. J. Wiley, J. Kang, *Advanced Science* **2022**, *9*, 24 2201111.
- [29] N. Matsuhisa, M. Kaltenbrunner, T. Yokota, H. Jinno, K. Kuribara, T. Sekitani, T. Someya, *Nature Communications* **2015**, *6*, 1 7461.
- [30] N. Karim, S. Afroz, S. Tan, P. He, A. Fernando, C. Carr, K. S. Novoselov, *ACS Nano* **2017**, *11*, 12 12266.
- [31] B. Wang, A. Facchetti, *Advanced Materials* **2019**, *31*, 28 1901408.
- [32] S. Afroz, N. Karim, Z. Wang, S. Tan, P. He, M. Holwill, D. Ghazaryan, A. Fernando, K. S. Novoselov, *ACS Nano* **2019**, *13*, 4 3847.
- [33] B. Wang, X. Lai, H. Li, C. Jiang, J. Gao, X. Zeng, *ACS Applied Materials & Interfaces* **2021**, *13*, 19 23020.
- [34] T. Stockinger, D. Wirthl, G. Mao, M. Drack, R. Pruckner, S. Demchyshyn, M. Steiner, F. Egger, U. Müller, R. Schwödiauer, S. Bauer, N. Arnold, M. Kaltenbrunner, *Advanced Materials* **2021**, *33*, 37 2102736.
- [35] V. Orts Mercadillo, K. C. Chan, M. Caironi, A. Athanassiou, I. A. Kinloch, M. Bissell, P. Cataldi, *Advanced Functional Materials* **2022**, *32*, 38 2204772.
- [36] S. Tan, M. R. Islam, H. Li, A. Fernando, S. Afroz, N. Karim, *Advanced Sensor Research* **2022**.
- [37] X. Zhang, X. Wang, Z. Lei, L. Wang, M. Tian, S. Zhu, H. Xiao, X. Tang, L. Qu, *ACS Applied Materials & Interfaces* **2020**, *12*, 12 14459.
- [38] S. Afroz, S. Tan, A. M. Abdelkader, K. S. Novoselov, N. Karim, *Advanced Functional Materials* **2020**, *30*, 23 2000293.
- [39] B. Niu, T. Hua, B. Xu, *ACS Sustainable Chemistry & Engineering* **2020**, *8*, 34 12842.
- [40] P. Cataldi, A. Athanassiou, I. S. Bayer, *Applied Sciences* **2018**, *8*, 9 1438.
- [41] C. Wang, K. Xia, H. Wang, X. Liang, Z. Yin, Y. Zhang, *Advanced Materials* **2019**, *31*, 9 1801072.
- [42] P. Cataldi, D. G. Papageorgiou, G. Pinter, A. V. Kretinin, W. W. Sampson, R. J. Young, M. Bissell, I. A. Kinloch, *Advanced Electronic Materials* **2020**, *6*, 9 2000429.
- [43] X. Wu, P. Steiner, T. Raine, G. Pinter, A. Kretinin, C. Kocabas, M. Bissell, P. Cataldi, *Advanced Electronic Materials* **2020**, *6*, 7 2000232.
- [44] P. Cataldi, P. Steiner, T. Raine, K. Lin, C. Kocabas, R. J. Young, M. Bissell, I. A. Kinloch, D. G. Papageorgiou, *ACS Applied Polymer Materials* **2020**, *2*, 8 3525.
- [45] P. Cataldi, M. Liu, M. Bissell, I. A. Kinloch, *Advanced Materials Technologies* **2022**, *7*, 11 2200025.

- [46] L.-X. Liu, W. Chen, H.-B. Zhang, Q.-W. Wang, F. Guan, Z.-Z. Yu, *Advanced Functional Materials* **2019**, *29*, 44 1905197.
- [47] C. Ye, J. Ren, Y. Wang, W. Zhang, C. Qian, J. Han, C. Zhang, K. Jin, M. J. Buehler, D. L. Kaplan, S. Ling, *Matter* **2019**, *1*, 5 1411.
- [48] C. Wang, T. Yokota, T. Someya, *Chemical Reviews* **2021**, *121*, 4 2109.
- [49] M. Dulal, S. Afroz, J. Ahn, Y. Cho, C. Carr, I.-D. Kim, N. Karim, *ACS Nano* **2022**, *16*, 12 19755.
- [50] X. Liang, H. Li, J. Dou, Q. Wang, W. He, C. Wang, D. Li, J.-M. Lin, Y. Zhang, *Advanced Materials* **2020**, *32*, 31 2000165.
- [51] P. Cataldi, M. Cassinelli, J. A. Heredia-Guerrero, S. Guzman-Puyol, S. Naderizadeh, A. Athanassiou, M. Caironi, *Advanced Functional Materials* **2020**, *30*, 3 1907301.
- [52] W.-Y. Ko, L.-T. Huang, K.-J. Lin, *Sensors and Actuators A: Physical* **2021**, *317* 112437.
- [53] M. Dammak, Y. Fourati, Q. Tarrés, M. Delgado-Aguilar, P. Mutjé, S. Boufi, *Industrial Crops and Products* **2020**, *144* 112061.
- [54] C. Aversa, M. Barletta, G. Cappiello, A. Gisario, *European Polymer Journal* **2022**, 111304.
- [55] J. Jian, Z. Xiangbin, H. Xianbo, *Advanced Industrial and Engineering Polymer Research* **2020**, *3*, 1 19.
- [56] F. G. Delolo, E. N. dos Santos, E. V. Gusevskaya, *Green Chemistry* **2019**, *21*, 5 1091.
- [57] M. Najafi, M. Zahid, L. Ceseracciu, M. Safarpour, A. Athanassiou, I. S. Bayer, *Journal of Materials Research and Technology* **2022**, *18* 5197.
- [58] S. Venkatesan, Q. Chen, E. C. Ngo, N. Adhikari, K. Nelson, A. Dubey, J. Sun, V. Bommisetty, C. Zhang, D. Galipeau, Q. Qiao, *Energy Technology* **2014**, *2*, 3 269.
- [59] W. Kim, M. Lorenzini, K. Kapıcıoğlu, A. Ajoudani, *IEEE Robotics and Automation Letters* **2018**, *3*, 4 4179.
- [60] W. Kim, V. R. Garate, J. M. Gandarias, M. Lorenzini, A. Ajoudani, *IEEE Transactions on Haptics* **2021**, *15*, 1 200.
- [61] M. Lorenzini, S. Ciotti, J. M. Gandarias, S. Fani, M. Bianchi, A. Ajoudani, In *31st IEEE International Conference on Robot and Human Interactive Communication (RO-MAN)*. **2022** 707–713.
- [62] M. Lorenzini, J. M. Gandarias, L. Fortini, W. Kim, A. Ajoudani, In *9th IEEE RAS/EMBS International Conference for Biomedical Robotics and Biomechatronics (BioRob)*. **2022** 01–06.
- [63] D. Sirintuna, I. Ozdamar, J. M. Gandarias, A. Ajoudani, *arXiv preprint arXiv:2302.02881* **2023**.
- [64] P. Cataldi, S. Dussoni, L. Ceseracciu, M. Maggiali, L. Natale, G. Metta, A. Athanassiou, I. S. Bayer, *Advanced Science* **2018**, *5*, 2 1700587.
- [65] X. Li, X. Ai, H. Pan, J. Yang, G. Gao, H. Zhang, H. Yang, L. Dong, *Polymers for Advanced Technologies* **2018**, *29*, 6 1706.
- [66] F. Wu, M. Misra, A. K. Mohanty, *RSC advances* **2019**, *9*, 5 2836.
- [67] J. Zhang, V. Hirschberg, D. Rodrigue, *International Journal of Fatigue* **2022**, *159* 106798.
- [68] A. Heiden, D. Preninger, L. Lehner, M. Baumgartner, M. Drack, E. Woritzka, D. Schiller, R. Gerstmayr, F. Hartmann, M. Kaltenbrunner, *Science Robotics* **2022**, *7*, 63 eabk2119.

- [69] P. Cataldi, L. Ceseracciu, A. Athanassiou, I. S. Bayer, *ACS Applied Materials & Interfaces* **2017**, *9*, 16 13825.
- [70] Y. Zhang, H. Ren, H. Chen, Q. Chen, L. Jin, W. Peng, S. Xin, Y. Bai, *ACS Applied Nano Materials* **2021**, *4*, 9 9709.
- [71] L. Ceseracciu, J. A. Heredia-Guerrero, S. Dante, A. Athanassiou, I. S. Bayer, *ACS Applied Materials & Interfaces* **2015**.
- [72] Y. Huang, M. J. Griffin, *Ergonomics* **2014**, *57*, 8 1244.
- [73] S.-W. Hwang, J.-K. Song, X. Huang, H. Cheng, S.-K. Kang, B. H. Kim, J.-H. Kim, S. Yu, Y. Huang, J. A. Rogers, *Advanced Materials* **2014**, *26*, 23 3905.
- [74] L. Yin, H. Cheng, S. Mao, R. Haasch, Y. Liu, X. Xie, S.-W. Hwang, H. Jain, S.-K. Kang, Y. Su, J. A. Rogers, *Advanced Functional Materials* **2014**, *24*, 5 645.
- [75] Y. Zhang, F. Liu, Y. Zhang, J. Wang, D. D'Andrea, J. B. Walters, S. Li, H.-J. Yoon, M. Wu, S. Li, Z. Hu, T. Wang, J. Choi, K. Bailey, E. Dempsey, K. Zhao, A. Lantsova, Y. Bouricha, I. Huang, H. Guo, X. Ni, Y. Wu, G. Lee, F. Jiang, Y. Huang, C. K. Franz, J. A. Rogers, *Proceedings of the National Academy of Sciences* **2023**, *120*, 11 e2217734120.
- [76] P. Cataldi, P. Steiner, M. Liu, G. Pinter, A. Athanassiou, C. Kocabas, I. A. Kinloch, M. A. Bissett, *Advanced Functional Materials* **2023**, 2301542.
- [77] S. Choi, K. J. Kuchenbecker, *Proceedings of the IEEE* **2012**, *101*, 9 2093.
- [78] D. Wang, C. Peng, N. Afzal, W. Li, D. Wu, Y. Zhang, *IEEE Transactions on Haptics* **2017**, *11*, 1 97.